Chemical Science

ROYAL SOCIETY OF CHEMISTRY

EDGE ARTICLE

View Article Online
View Journal | View Issue

Cite this: *Chem. Sci.*, 2025, **16**, 8697

All publication charges for this article have been paid for by the Royal Society of Chemistry

Establishing the stability number descriptor for Fe–N–C fuel cell electrocatalysts†

Yu-Ping Ku, *[ab] Kavita Kumar, [a] Antoine Bonnefont, [c] Li Jiao, [d] Marco Mazzucato, [e] Christian Durante, [e] Frédéric Jaouen [d] and Serhiy Cherevko *[a]

Fe–N–C electrocatalysts demonstrate high potential in catalyzing oxygen reduction reaction (ORR) in polymer electrolyte fuel cells, yet the bottleneck for their application is their moderate stabilities. In our previous work, we discovered a linear correlation between the rates of ORR and Fe dissolution in alkaline media at room temperature, and the stability (*S*-) number descriptor that reflects this correlation was introduced. On the way toward further generalization and establishment of this descriptor, we investigate the effect of pH, potential, current density, and temperature on the dissolution behavior of various representative Fe–N–C electrocatalysts. It is shown that the *S*-number concept is also applicable for ORR and Fe dissolution in alkaline electrolytes at 70 °C. It is more challenging to apply the *S*-number in acidic media, where the *S*-number is a function of ORR current density. A kinetic model is introduced, showing that the local pH inside the catalyst layer rises significantly with increasing current densities. The pH dependence of the *S*-number explains the results in acidic electrolytes. Accounting for such a dependence, the *S*-number descriptor can also benchmark Fe–N–C stability in acidic electrolytes. It is considered that this concept can also be extended to other reactions, allowing more rational activity and stability screening of electrocatalysts.

Received 21st January 2025
Accepted 12th April 2025

DOI: 10.1039/d5sc00547g

rsc.li/chemical-science

1. Introduction

Fe–N–C catalysts are the most promising alternative to platinum-group-metal (PGM) materials used as the oxygen reduction reaction (ORR) catalysts at cathodes of proton exchange membrane fuel cells (PEMFCs) and anion exchange membrane fuel cells (AEMFCs). However, Fe–N–C materials still suffer from unsatisfactory durability, particularly in acidic environments of PEMFCs. In order to develop mitigation strategies that improve their durability, the fundamental understanding of the degradation mechanisms still needs to be deepened. Hence, the current knowledge of the degradation mechanisms of Fe–N–C catalysts has been summarized in detail in ref. 1 and briefly presented here as follows.

The relevant potential (E) ranges for ORR catalysts are 0.6 V_{RHE} < E < open circuit potential (OCP) during the operating mode and OCP < E < 1.5 V_{RHE} in start–stop events.[2] The primary degradation mechanism of Fe–N–C catalysts in the E range OCP < E < 1.5 V_{RHE} is the electrochemical oxidation of the N–C matrix,[3–8] producing either O-containing functional groups or gaseous NO_x/CO_x. The compromised integrity of the N–C matrix may lead to Fe demetallation,[8,9] followed by partial re-deposition as iron oxides,[8] and the destruction of the catalyst layer's porous structure.[10] On the other hand, the main degradation mechanisms during ORR (0.6 V_{RHE} < E < OCP) are the reactive oxygen species (ROS) attack[11–13] and Fe demetallation (or Fe leaching/dissolution).[9,14–16] The ROS are usually produced by Fenton reactions between Fe species and the ORR intermediate/byproduct H_2O_2. The ROS could oxidize the carbon surface (faster in acidic than in alkaline media, due to different ROS species formed at different pH), resulting in a decreased turnover frequency (TOF) of FeN_xC_y sites.[11–13] Additionally, the higher TOF contributed by the more basic N-groups after NH_3-pyrolysis may reduce due to their protonation and subsequent anion adsorption.[17] Besides a decreased average TOF of FeN_xC_y sites, the demetallation of Fe from such sites during operation can decrease the active site density (SD) and thus also decrease the ORR activity of the active layer. Fe demetallation can be indirectly triggered by the electrochemical oxidation of the N–C matrix (OCP < E < 1.5 V_{RHE}) or directly

[a]*Forschungszentrum Jülich GmbH, Helmholtz-Institute Erlangen-Nürnberg for Renewable Energy (IET-2), Cauerstraße 1, 91058 Erlangen, Germany. E-mail: yupingku427@gmail.com; s.cherevko@fz-juelich.de*

[b]*Department of Chemical and Biological Engineering, Friedrich-Alexander University Erlangen-Nürnberg, Egerlandstraße 3, 91058 Erlangen, Germany*

[c]*Univ. Grenoble Alpes, Univ. Savoie-Mont-Blanc, CNRS, Grenoble-INP, LEPMI, 38000 Grenoble, France*

[d]*Institut Charles Gerhardt Montpellier, Univ. Montpellier, CNRS, ENSCM, 1919 route de Mende, F-34293 Montpellier, France*

[e]*Department of Chemical Sciences, University of Padova, via Marzolo 1, 35131, Padova, Italy*

† Electronic supplementary information (ESI) available. See DOI: https://doi.org/10.1039/d5sc00547g

induced by the ORR (0.6 V_{RHE} < E < OCP). The rate of Fe dissolution in the E range 0.6 V_{RHE} < E < OCP could vary with the chemical nature of the Fe species,[14,16,18] the pH value of the environment,[14] the electrochemical potential,[9,15] the temperature,[9] and the presence/absence of O_2.[15] A fraction of dissolved Fe species might re-deposit on the catalytic surface as Fe oxide clusters.[16,19,20] Such clusters have some ORR activity in alkaline media, and may have synergy with FeN_xC_y sites.[19] Consequently, the dominant degradation mechanisms in the operating mode of PEMFCs are the ROS attack and Fe dissolution. In contrast, the main degradation mechanism in AEMFCs in operation is Fe dissolution, while deposition as Fe oxides could contribute to mitigating the ORR activity loss.[19]

Hence, in studies on the durability of Fe–N–C catalysts, the fate of the active Fe species has been one of the main focuses. The initial active Fe species can be diverse, including atomically dispersed Fe in N–C structure (FeN_xC_y sites), Fe-carbide particles protected by N-doped graphene layers (Fe_3C@N–C), *etc.* As these active Fe species possess varied activities and stabilities, Fe–N–C catalysts with mainly a certain type of Fe species are ideal for fundamental studies. Furthermore, the changes in the Fe species in a membrane electrode assembly can be observed post-mortem by Mössbauer spectroscopy. Alternatively, Fe dissolution can be detected *in situ* by coupling an electrochemical cell, such as a scanning flow cell (SFC) or a gas diffusion electrode (GDE) half-cell, to an inductively coupled plasma mass spectrometer (SFC-ICP-MS[9,14] or GDE-ICP-MS,[8,15,21] respectively), revealing the dissolution rate as a function of the applied electrochemical protocol.

In order to characterize the activity *vs.* stability of a given electrochemical catalyst, the stability (*S*-) number was first introduced for Ir-based catalysts for oxygen evolution reaction (OER) and defined as the ratio between the amount of evolved O_2 and the amount of dissolved iridium.[22] The higher the *S*-number is, the more O_2 can be evolved per dissolved iridium. Moreover, the *S*-number was found to be relatively constant over wide ranges of current density and potential, suggesting that the Ir dissolution and OER mechanisms are interconnected, potentially through a common intermediate.[23] In this line, a linear correlation between the rates of Fe dissolution and charge transfer during ORR at current densities up to −125 mA cm^{-2} was revealed for both Fe_3C@N–C-rich and FeN_xC_y-rich Fe–N–C catalysts in alkaline media at room temperature (RT) in the potential range 0.57–0.87 V_{RHE}, in our previous work using GDE-ICP-MS.[15] Based on this observation, the *S*-number descriptor was also introduced for Fe–N–C catalysts in the testing condition and defined as the number of electrons exchanged in the ORR per dissolved Fe cation. In our previous work,[15] we reported the ORR charge-normalized amount of dissolved Fe species, which is inversely proportional to the *S*-number.

The *S*-number can be a powerful stability descriptor for Fe–N–C catalysts, especially at the beginning of life when their states are still close to their pristine states, for which the Fe species can be well identified from *ex situ* characterization of the catalyst or active layer. When the dissolved Fe is mainly from the most active Fe species, such as the FeN_xC_y sites, the *S*-number represents an average of how many times ORR faradaic charge transfer occurs among a large amount of FeN_xC_y sites before an Fe ion dissolves from one of the active sites. However, after a long aging protocol or accelerated stress test (AST), the amount of dissolved Fe species can be significant, and the amount of re-deposited Fe species as well. In turn, the Fe dissolution from such inactive (or less active) redeposited Fe species could then contribute to the amounts of leached Fe measured after the aging protocol or AST. The resulting *S*-number measured on such a modified Fe–N–C surface might then no longer correspond to the stability of the FeN_xC_y sites. Hence, interpreting *S*-numbers obtained from data measured before, during, and after ASTs must be proceeded with caution.

The observed constant *S*-number (*i.e.* the same linear correlation between the amount of the dissolved Fe and the number of electrons exchanged in the ORR) across a range of current densities for Fe–N–C materials in alkaline media suggests that the destabilization of the active Fe species is predominantly due to their less stable intermediate state(s) during the ORR catalytic cycle. It can be expected that the more dominant this demetallation mechanism is, the stronger the correlation between the amount of the dissolved Fe and the number of electrons exchanged in the ORR is (or the more constant the *S*-number is). In other words, if the *S*-number varies with the electrochemical potential or current density, then other degradation mechanisms that are potential-dependent or some current-density-dependent variables should be considered. For example, the faradaic efficiency of H_2O_2 could vary with potential,[11,24] and so would the following ROS attack. The ROS may oxidize the matrix around FeN_xC_y sites, which may not only reduce their TOF but also strengthen the Fe–N bonds of FeN_4C_{10} sites or weaken the Fe–N bonds of FeN_4C_{12} sites.[11,25] Moreover, the oxidation state of the Fe of FeN_4C_{12} sites switches from +III at 0.8 V to +II at 0.2 V, whereas that of FeN_4C_{10} sites do not.[16] Hence, the stability of FeN_4C_{12} sites may be potential-dependent. As another example, an elevated ORR current density means faster consumption of H^+ in acidic or production of OH^- in alkaline catalyst layers. If these processes are faster than the migration of H^+ from, or OH^- to, the bulk electrolytes, then the local pH values in the catalyst layers would increase.[26] The increased local pH can be a critical factor for the stability of FeN_xC_y sites because they have been theoretically predicted[27] and experimentally proven[14] more stable in alkaline than in acidic media in the E range 0.6 < E < 1.0 V_{RHE}. Hence, before using the *S*-number to compare Fe–N–C catalysts in other conditions, the linear correlation between the amount of dissolved Fe species and the number of electrons exchanged in the ORR in those conditions should be verified.

In this study, we investigate for the first time the use of the *S*-number for Fe–N–C materials in acidic and alkaline media, at both room and elevated temperatures, using GDE-ICP-MS. This stability descriptor was validated by correlating the amount of dissolved Fe with the number of electrons exchanged in the ORR. Relevant conditions, such as high current density (−100 mA cm^{-2}), high temperature (70 ± 6 °C), and potential range 0.55–1.0 V_{RHE}, were applied in the GDE setup. The study was

systematically conducted on a commercial Fe–N–C catalyst from Pajarito Powder (made by silica hard template method), and on two laboratory Fe–N–C materials (one was derived from ZIF-8 and the other from steam-treated carbon black). While the materials differ by their synthesis methods, all three are rich in FeN_xC_y sites and poor in Fe side-phases. Our results point toward the *S*-number as a suitable stability descriptor for Fe–N–C catalysts in alkaline media not only at RT but also at 70 °C. This descriptor could also be meaningful in acidic media if the impact of the increased local pH induced by a faster ORR rate is considered, as supported by experimental and kinetic modeling results in this study.

2. Experimental

2.1 Fe–N–C catalysts

There are three FeN_xC_y-rich Fe–N–C catalysts studied in this work: one commercial Fe–N–C catalyst (Pajarito Powder PMF-D14401, noted as PAJ_FeN_xC_y in this work) and two laboratory-synthesized Fe–N–C catalysts, CNRS_FeN_xC_y from CNRS – University of Montpellier (labeled as $Fe_{0.5}$-dry in ref. 28), and UNIPD_FeN_xC_y from University of Padova (labeled as FNCBSt10 in ref. 29). The synthesis of CNRS_FeN_xC_y used a sacrificial metal–organic framework, ZIF-8, to obtain its porous structure.[28] In contrast, the synthesis of UNIPD_FeN_xC_y employed an activation procedure with steam on a commercial carbon black as the carbon support to adjust its porous structure.[29] The ^{57}Fe Mössbauer spectra of PAJ_FeN_xC_y and CNRS_FeN_xC_y were provided in ref. 8 and 28, respectively, testifying that the Fe species in these two catalysts are mostly FeN_xC_y species. Moreover, a detailed characterization of UNIPD_FeN_xC_y was provided in ref. 29, where its transmission electron microscopy images showed very few isolated Fe nanoparticles covered with carbon shells. Thus, UNIPD_FeN_xC_y is also considered an FeN_xC_y-rich Fe–N–C catalyst.

2.2 Electrode preparation

In this work, when doctor-blade coating an Fe–N–C catalyst layer (CL), a certain thickness of a prepared ink was applied on a gas diffusion medium (H23C8, Freudenberg, 3 × 3 cm^2), using an automated film applicator (ZAA 2300, Zehntner) where the plate was set to 30 °C. For the CLs tested in 0.1 M NaOH (Merck Suprapure), the ink was composed of 7.7 wt% of Fe–N–C catalyst (see Section 2.1), 3.3 wt% of a commercial ionomer (Aemion HNN5-00-X, Ionomr), and 89.0 wt% of 1-propanol (≧99.9%, Sigma-Aldrich). For the CLs tested in 0.1 M $HClO_4$ (Suprapur, Sigma-Aldrich), the ink consisted of 6.2 wt% of Fe–N–C catalyst, 44.0 wt% of a commercial Nafion solution (D2021, Fuel Cell Store, containing 20 wt% Nafion), and 49.8 wt% of 2-propanol (Supelco, EMSURE). The ink preparation always started with thoroughly mixing the Aemion ionomer or Nafion solution with the (additional) solvent. Then, the Fe–N–C catalyst was added to this solution. The resulting ink was first stirred for one hour, then sonicated for one hour (100 W VWR Ultrasonic Cleaner USC 500 THD, temperature ≤30 °C), and finally stirred until being applied on the gas diffusion medium. The applied ink

Table 1 The testing conditions: the electrolyte and its temperature ($T_{electrolyte}$); the gas purged from the side of the gas diffusion layer (O_2, humidified or not), its temperature (T_{gas}) and flow rate. The catalyst loading and the thickness of each catalyst layer (CL). The collection efficiency (CE) and the electrolyte flow rate during each measurement. The calibrated potential of the reference electrode ($E_{Ag/AgCl}$) at $T_{electrolyte}$. The details of the 200-cycle ASTs: two galvanostatic steps in each cycle, 3 seconds at "*j*" mA cm^{-2} and 3 seconds at −0.1 mA cm^{-2}; and the potential *E* range resulting from the applied "*j*" mA cm^{-2}

	UNIPD_FeN_xC_y		PAJ_FeN_xC_y		CNRS_FeN_xC_y		
Electrolyte	0.1 M NaOH	0.1 M NaOH	0.1 M $HClO_4$	0.1 M NaOH	0.1 M NaOH	0.1 M $HClO_4$	
$T_{electrolyte}$, °C		67.0 ± 3.0	74.5 ± 0.5	71.0 ± 2.5		69.5 ± 2.5	
T_{gas}, °C	Room temperature	67.0 ± 7.0	71.5 ± 1.5	71.5 ± 0.5		73.5 ± 1.5	
Humidification/O_2 flow rate, mL min^{-1}	Non-humidified/50	Humidified/125	Humidified/125	Humidified/125		Humidified/125	
Loading, mg$_{Fe-N-C}$ cm^{-2}	0.42	0.64	1.00	0.61	0.98	0.98	0.82	0.80	0.98	1.01
Thickness of CL, μm	10.8	15.0	37.0	24.8	42.3	43.5	28.0	25.0	30.5	29.8
CE, %	19.8	22.6	26.4	28.7	27.8	41.2	26.6	26.5	20.4	17.8
Electrolyte flow rate, mL min^{-1}	0.18	0.18	0.23	0.22	0.24	0.24	0.23	0.21	0.22	0.21
$E_{Ag/AgCl}$, V_{RHE}	0.971 ± 0.001		0.944 ± 0.003		0.330 ± 0.001		0.943 ± 0.002		0.275 ± 0.011	
j, mA cm^{-2} in AST	−100		−100		−100		−100		−75	
E, V_{RHE} (resulting from the applied "*j*")	0.50–0.60		0.60–0.64		0.68–0.74		0.59–0.63		0.50–0.62	

was then dried at 60 °C, under 1 atm in the first hour and under reduced pressure in the second hour. The catalyst loadings are provided in Table 1. The CLs with Aemion were kept in 1 M KOH (EMSURE®, Merck) for three hours to exchange the I^- in as-received Aemion with OH^-, and the CLs with Nafion were kept in ultrapure H_2O for one hour to wet the CLs, followed by a thorough washing step with ultrapure H_2O repeated three times before the measurements.

2.3 GDE-ICP-MS measurements

To detect the online dissolution from a GDE sample during electrochemical protocols, the technique GDE-ICP-MS (ICP-MS: Perkin Elmer, NexION™ 350X) has been developed in our previous works,[8,15,30] which provided the detailed methodology, including the calculation of the collection efficiency (CE) (see eqn (1)). The CE values in this work are listed in Table 1. A scheme of the GDE-ICP-MS setup is provided as Scheme 1, which was originally adapted from Fig. S1 in ref. 30 and was already published in ref. 15.

$$CE = m_{ICP\text{-}MS}/(m_{bulk,end} - m_{bulk,start} + m_{ICP\text{-}MS} + m_{tube}) \quad (1)$$

In eqn (1), $m_{ICP\text{-}MS}$, $m_{bulk,end} - m_{bulk,start}$, and m_{tube} refer to the amounts of the dissolved metal that were collected into the ICP-MS, accumulated in the bulk electrolyte, and stayed in the tube where the electrolyte recirculated during the measurement for a heating purpose, respectively.

The *S*-number is defined as the number of electrons exchanged in the ORR divided by the number of dissolved Fe, that is:

$$S\text{-number} = (|j| \times t \div e)/(n_{Fe,diss.} \times N_A) \quad (2)$$

In eqn (2), j, t, and e refer to current density, step duration, and elementary charge, respectively, and $n_{Fe,diss.}$ and N_A are the amount of the dissolved Fe in mole cm^{-2} and the Avogadro constant, respectively.

Moreover, for an ICP-MS using Ar plasma to detect ^{56}Fe, operating the ICP-MS in dynamic reaction cell mode using CH_4 (N45, Air Liquide) is required for a higher ratio of ^{56}Fe to $^{40}Ar^{16}O^+$ (signal-to-noise ratio), as CH_4 reacts with $^{40}Ar^{16}O^+$ faster than with ^{56}Fe. The long-term status of the ICP-MS was tracked with an internal standard solution containing a constant concentration of ^{74}Ge (100 μg L^{-1} for the measurements of UNIPD_FeN_xC_y and 2.5 μg L^{-1} for the others, Merck Centripur) in 1 wt% HNO_3 (ROTIPURAN®Supra, ROTH). Before every measurement, a four-point calibration curve was created with a blank electrolyte and three standard solutions (0, 1, 5, 25 μg_{Fe} L^{-1}). The standard solutions were prepared in two steps. First, the Merck Centripur ICP standard solution (1000 mg_{Fe} L^{-1}) was diluted to 1 mg_{Fe} L^{-1} with 1 wt% HNO_3. Then, the 1 mg_{Fe} L^{-1} middle standard solution was diluted with the blank electrolyte to the desired concentrations.

In this work, PAJ_FeN_xC_y and CNRS_FeN_xC_y were tested in both 0.1 M $HClO_4$ and 0.1 M NaOH at 70 ± 6 °C (HT) (see

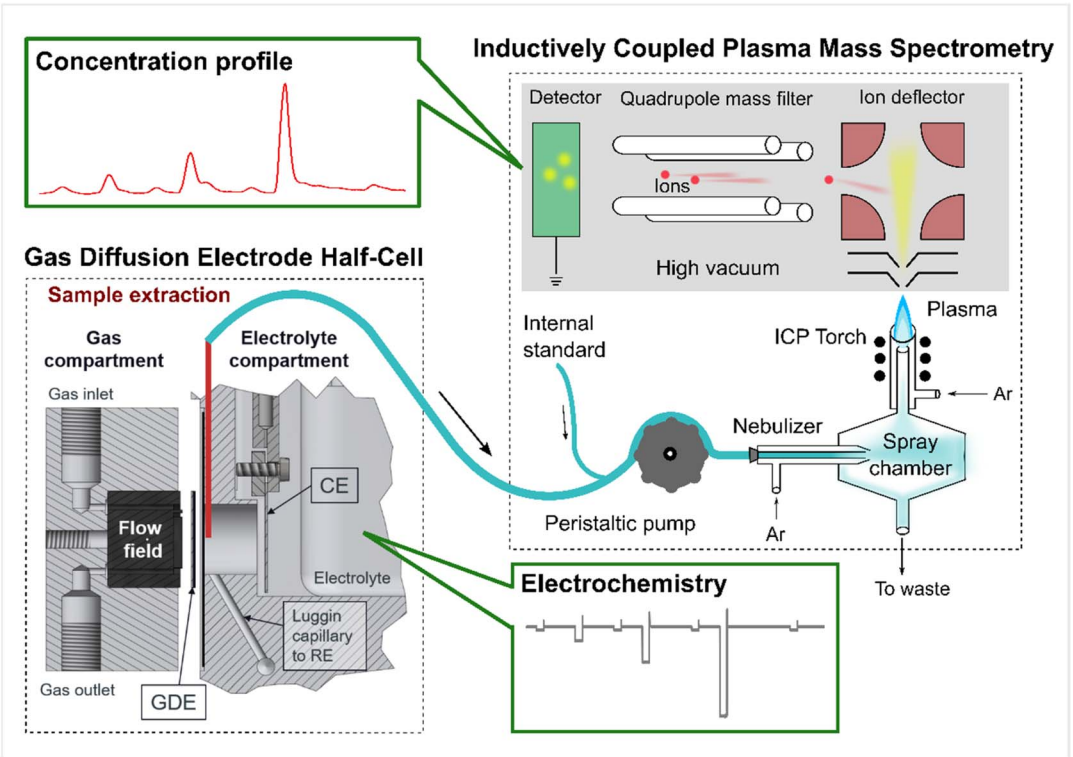

Scheme 1 An illustration of the gas diffusion electrode (GDE) half-cell coupled to an inductively coupled plasma mass spectrometry (GDE-ICP-MS) setup. The scheme was originally adapted from Fig. S1 in ref. 30 (an open access article). This adapted scheme has been published in our previous work.[15]

Table 1) while UNIPD_FeN$_x$C$_y$ was tested in 0.1 M NaOH at RT. During each online measurement, O_2 was provided from the gas-diffusion-layer side of the GDE sample with a flow rate, whose value is provided in Table 1. Meanwhile, an additional 50 mL min^{-1} Ar flow was purged into the electrolyte for stirring, which from experience is good for the signal-to-noise ratio of the online dissolution profiles. For all electrochemical protocols in the three testing conditions (Alkaline-RT, Alkaline-HT, and Acidic-HT), an activity test was always performed before and after a 200-cycle accelerated stress test (AST), each cycle of which consisted of two galvanostatic steps, 3 seconds at "j" mA cm^{-2} (the j-value for all experiments is listed in Table 1) and 3 seconds at -0.1 mA cm^{-2}. For each condition, the activity test is illustrated in Scheme 2. The exact sets of chosen current densities in the activity tests vary slightly among the conditions to cover the potential and current density ranges that are relevant to fuel-cell applications. During the activity tests, the galvanostatic steps in Acidic-HT were shortened to only 10 s due to the recognized more rapid degradation of Fe–N–C catalysts in acidic media, while in Alkaline-HT and Alkaline-RT, the galvanostatic steps were prolonged to 40 s because of the lower signal-to-noise ratio in alkaline media. The measured electrochemical potential was 100% post-measurement *iR*-corrected, with respect to a reversible hydrogen electrode (RHE). For the *iR*-correction, the uncompensated resistance (R_u) was obtained with electrochemical impedance spectroscopy at each applied current density. The calibration of the reference electrode Ag/AgCl (Metrohm, inner compartment: 3 M KCl, outer compartment: 3 M KCl for alkaline measurements or 0.1 M $HClO_4$ for acidic measurements) with respect to a RHE was performed every day at the temperature of interest, of which the results are provided in Table 1. For the calibration of the reference electrode at an elevated temperature, the used electrochemical cell was put in a water bath that was maintained at the targeted temperature. The counter electrode was an expanded sheet of Ti coated with Ir/Ta mixed metal oxide (METAKEM). The geometric area of the GDE sample S_{GDE} was 2.01 cm^2. To show the reproducibility of the result, each measurement was conducted twice, each time on a fresh GDE sample.

2.4 Kinetic modeling

The concentration profiles of proton in the aqueous phase (C_H), Fe^{III} (C_{Fe}) and hydroxides ions (C_{OH}) as a function of time (t) and space (x) are modelled by solving a system of partial differential equations describing the effect of mass transport and of reactions in the catalyst layer and in the electrolyte. In a first approximation, the gaseous oxygen concentration in the catalyst layer and the amount of FeN$_x$C$_y$ sties are assumed to be constant. The local ORR rate is equal to $k_r \times C_H(x, t)$ where k_r is the ORR rate constant. The Fe dissolution rate from FeN$_x$C$_y$ sites is assumed to be the product of the ORR rate, $k_r \times C_H(x, t)$, and a constant dissolution coefficient $k_{dis} = 4.6 \times 10^{-5}$.

In addition to the ORR, the reactions considered in the model are:

(a) The self-ionization of water, $H_2O \Leftrightarrow H^+ + OH^-$ ($k_{fw} = 1.4 \times 10^{-3}$ M s^{-1}, $k_{bw} = 7 \times 10^{10}$ M^{-1} s^{-1})

(b) The Fe precipitation: $Fe^{3+} + 3H_2O \Leftrightarrow Fe(OH)_3 + 3H^+$ (solubility constant of $Fe(OH)_3$, $K_s = 1.0 \times 10^{-42}$ at 70 °C, $k_d = 0.01$ s^{-1}, $k_p = 0.8$ cm^6 mol^{-2} s^{-1})

Thus, the set of partial differential equations describing the evolution of the concentration profiles in the catalyst layer can thus be expressed as:

$$\frac{\partial C_{Fe}}{\partial t} = D_{Fe,eff}\,\frac{\partial^2 C_{Fe}}{\partial x^2} + k_{dis}\,k_r C_H + k_d C_H{}^3 - k_p C_{Fe} \quad (3)$$

$$\frac{\partial C_H}{\partial t} = D_{H,eff}\frac{\partial^2 C_H}{\partial x^2} - k_r C_H - 3\left(k_d C_H{}^3 - k_p C_{Fe}\right) + k_{fw} - k_{bw} C_H C_{OH} \quad (4)$$

$$\frac{\partial C_{OH}}{\partial t} = D_{OH,eff}\frac{\partial^2 C_{OH}}{\partial x^2} + k_{fw} - k_{bw} C_H C_{OH} \quad (5)$$

with $D_{Fe,eff} = 6 \times 10^{-7}$ cm^2 s^{-1} and $D_{H,eff} = 3.5 \times 10^{-5}$ cm^2 s^{-1}.

The system of partial differential equations is solved for the initial conditions, at $t = 0$, $C_{Fe} = 0$ and $C_H = 10^{-1}$ M, $C_{OH} = 10^{-13}$ M. The following boundary conditions are used:

At the gas-phase/catalyst-layer interface at $x = 0$:

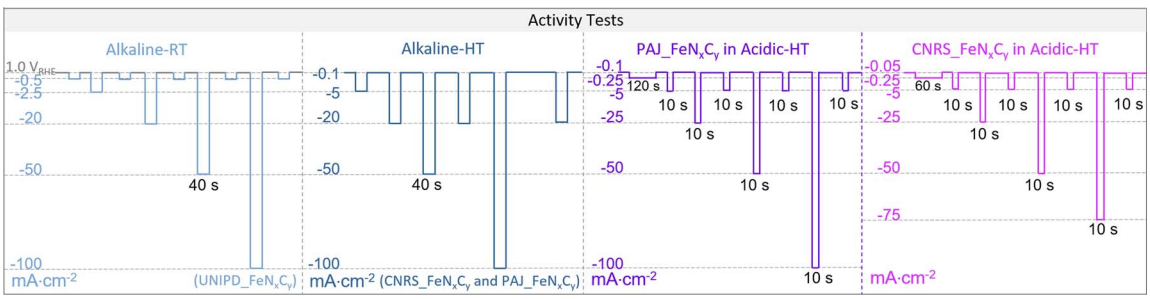

Scheme 2 The electrochemical protocols of the activity tests from left to right are for UNIPD_FeN$_x$C$_y$ in alkaline media at room temperature (Alkaline-RT, light blue), for both CNRS_FeN$_x$C$_y$ and PAJ_FeN$_x$C$_y$ in alkaline media at 70 ± 6 °C (Alkaline-HT, dark blue), for PAJ_FeN$_x$C$_y$ in acidic media at HT (Acidic-HT) (violet), and for CNRS_FeN$_x$C$_y$ in Acidic-HT (magenta). Except for the potentiostatic steps at 1.0 V_{RHE} as the near OCP in the Alkaline-RT protocol (marked in grey), all others were galvanostatic steps with the applied current densities noted on the left side of each protocol. Apart from the near OCP steps (1.0 V_{RHE}, -0.1 mA cm^{-2}, or -0.05 mA cm^{-2}) and the 120-s or 60-s steps at -0.25 mA cm^{-2} in Acidic-HT, the step durations of the others were set to 40 s, 40 s, and 10 s, in the activity test protocols in Alkaline-RT, Alkaline-HT, and Acidic-HT, respectively.

$$D_{\mathrm{Fe,eff}}\frac{\partial C_{\mathrm{Fe}}}{\partial x}=0$$

$$D_{\mathrm{H,eff}}\frac{\partial C_{\mathrm{H}}}{\partial x}=0$$

$$D_{\mathrm{OH,eff}}\frac{\partial C_{\mathrm{OH}}}{\partial x}=0$$

At the catalyst-layer/liquid-electrolyte interface at $x = 40$ μm: $D_{\mathrm{Fe,eff}}\frac{\partial C_{\mathrm{Fe}}}{\partial x} = m_{\mathrm{Fe}}(C_{\mathrm{Fe}} - C_{\mathrm{Fe,b}})$, where $C_{\mathrm{Fe,b}} = 10^{-7}$ M is the bulk concentration of dissolved iron in solution and $m_{\mathrm{Fe}} = 1.2 \times 10^{-3}$ cm s^{-1} is the mass transfer coefficient of the Fe in the solution.

$D_{\mathrm{H,eff}}\frac{\partial C_{\mathrm{H}}}{\partial x} = m_{\mathrm{H}}(C_{\mathrm{H}} - C_{\mathrm{H,b}})$, where $C_{\mathrm{H,b}} = 10^{-1}$ M is the bulk concentration of proton in solution and $m_{\mathrm{H}} = 1.2 \times 10^{-2}$ cm s^{-1} is the mass transfer coefficient of the protons.

The faradaic current is obtained by:

$$j_{\mathrm{F}} = F\int k_{\mathrm{r}} C_{\mathrm{H}}(x,t)\mathrm{d}x \quad (6)$$

where $F = 96\,485$ C mol^{-1} is the Faraday constant.

3. Results

In order to investigate to which extent the *S*-number is an appropriate stability descriptor for Fe–N–C catalysts in relevant conditions in PEMFCs and AEMFCs, two benchmark FeN_xC_y-rich Fe–N–C catalysts (CNRS_FeN_xC_y and PAJ_FeN_xC_y) were tested in O_2-saturated 0.1 M $HClO_4$ and 0.1 M NaOH at 70 ± 6 °C (Acidic-HT and Alkaline-HT, respectively) using a GDE-ICP-MS technique. The electrochemical protocols all involve an activity test pre-AST, a 200-cycle AST, and a repeated activity test post-AST. First, by comparing the pre-AST and post-AST Tafel plots, the drops in the ORR performance of the Fe–N–C catalyst layers can be observed in Fig. 1. Although the pristine ORR performance of both CNRS_FeN_xC_y and PAJ_FeN_xC_y varies with the electrolyte's pH value, the degradation in Acidic-HT (Fig. 1A and C) is clearly more severe than that in Alkaline-HT (Fig. 1B and D), agreeing with the theoretical and experimental results in the literature.[14,27]

As one of the main degradation mechanisms, Fe demetallation from Fe–N–C catalysts has been shown using SFC-ICP-MS to be more dramatic in acidic than in alkaline media.[14] Yet, the comparison in the literature was done at limited ORR current densities ($|j| \leq 10$ mA cm^{-2}), so this work uses GDE-ICP-MS to enable such a comparison at current densities up to −100 mA cm^{-2}. For example, Fig. 2 presents the profiles of online Fe dissolution from PAJ_FeN_xC_y for the Acidic-HT (see Fig. 2A–C) and Alkaline-HT (see Fig. 2D–F) conditions during the pre-AST activity tests, while the post-AST data is provided in Fig. S1 in the ESI.† As for CNRS_FeN_xC_y, the pre-AST and post-AST Fe dissolution profiles are shown in Fig. S2 and S3, respectively, in the ESI.† The dissolution peaks during the repeated

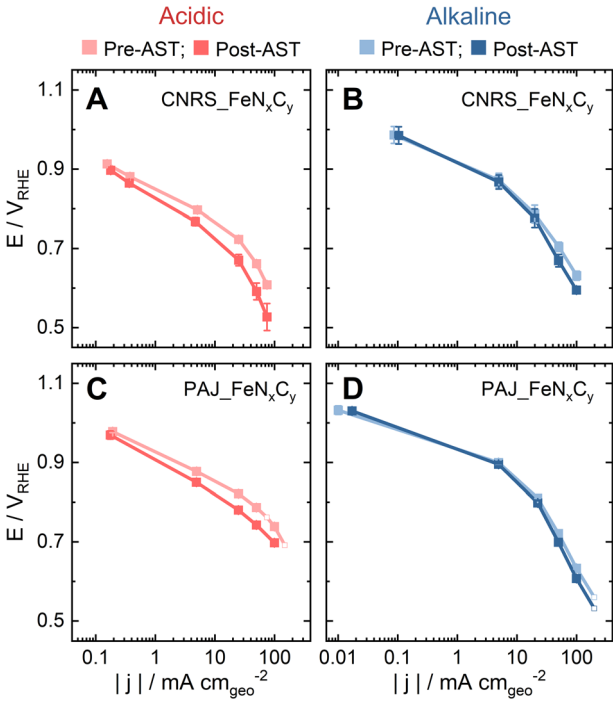

Fig. 1 Tafel plots of the pristine (pre-AST) and degraded (post-AST) Fe–N–C gas diffusion electrodes in O_2 at 70 ± 6 °C in the gas diffusion electrode half-cell (A & B) using CNRS_FeN_xC_y as the catalyst (A) in 0.1 M $HClO_4$ and (B) in 0.1 M NaOH; (C & D) using PAJ_FeN_xC_y as the catalyst (C) in 0.1 M $HClO_4$ and (D) in 0.1 M NaOH. The error bars represent the difference between the results of two experiments. The four blank square symbols show the data without repetition.

chronopotentiometry (CP) steps at −5 mA cm^{-2} in Acidic-HT in between the CP steps at various current densities (marked with grey shades) barely vary (see Fig. 2C and S4, the latter of which is in the ESI†). This verifies that the trend of the dissolution peaks at different current densities is hardly influenced by the step order in the Acidic-HT protocol. Compared to the Acidic-HT condition, the signal-to-noise ratio was lower and the background increased faster in Alkaline-HT. The standard deviation of the Fe background signals at the first near OCP step (before the first CP step of interest) is, on average, 1.85 pg_{Fe} s^{-1} mg_{Fe-N-C}^{-1} in Acidic-HT and 3.64 pg_{Fe} s^{-1} mg_{Fe-N-C}^{-1} in Alkaline-HT (almost double of the value obtained in Acidic-HT). Hence, it is not straightforward to draw the same conclusion from the dissolution peaks during the repeated CP steps at −20 mA cm^{-2} in the pre-AST measurements in Alkaline-HT although they do not suggest otherwise. Nevertheless, except for the repeated CP steps at −20 mA cm^{-2}, a step at a higher current density is always applied later to minimize the history effect. The trend of Fe dissolution in Acidic-HT is distinct from that in Alkaline-HT. In Alkaline-HT, the amount of the dissolved Fe species increased with the elevated current density. However, in Acidic-HT, the amount of the dissolved Fe species first climbed with the increased current density, reached a peak at −25 mA cm^{-2}, and then decreased with the rising current density. Because the step durations in these two protocols had to be different, which has been explained in the 2.3 section, it is not straightforward to

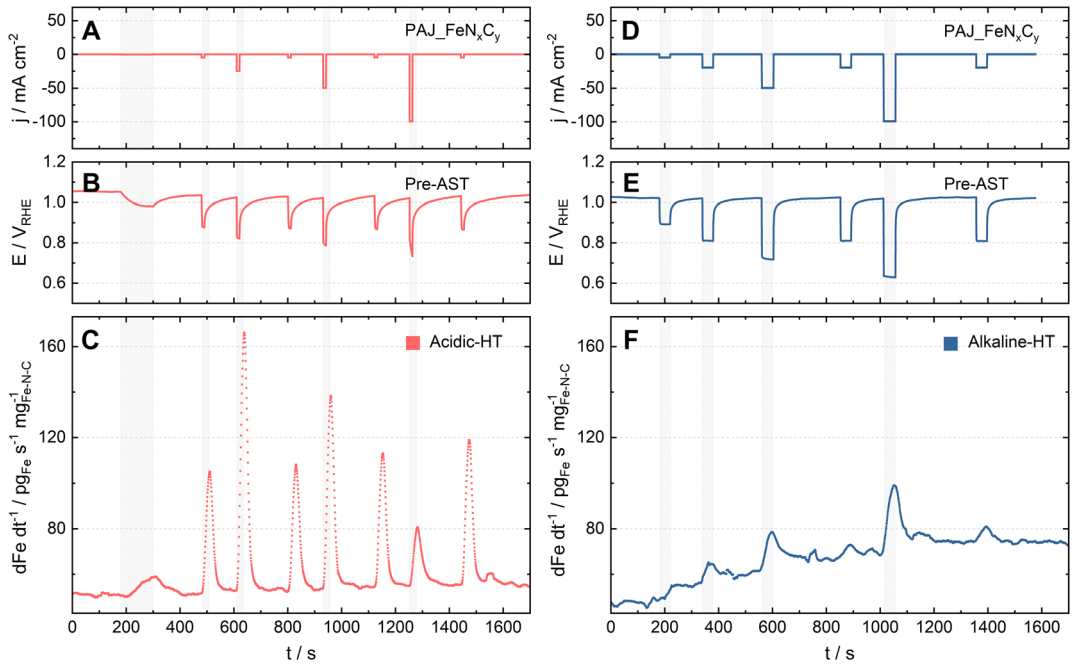

Fig. 2 Online GDE-ICP-MS results during the pre-AST measurements for PAJ_FeN$_x$C$_y$ (A–C) in 0.1 M $HClO_4$ at 70 ± 6 °C (Acidic-HT) and (D–F) in 0.1 M NaOH at HT (Alkaline-HT). (A & D) The current density profiles. (B & E) The potential profiles. (C & F) The corresponding online Fe dissolution profiles, which were normalized to the catalyst loading.

directly compare the Fe dissolution profiles (*e.g.* Fig. 2C and F). For easier comparison, the dissolution data will be henceforth shown as the *S*-numbers (see eqn (2)), which are calculated by dividing the number of electrons exchanged in the ORR by the number of the dissolved Fe species integrated from the dissolution profiles.

The *S*-numbers in Fig. 3 and 4 were all calculated from the Fe dissolution data set during the pre-AST activity tests to ensure the *S*-numbers correspond to the Fe–N–C states that were still close to the pristine state, where the dominant Fe species had been identified before potential formations of other Fe species in a longer testing.[16,19,31]

A similar trend of the *S*-number is observed for two FeN$_x$C$_y$-rich Fe–N–C catalysts (PAJ_FeN$_x$C$_y$ (ref. 8) and UNIPD_FeN$_x$C$_y$ (ref. 29)) in Alkaline-RT (see Fig. 3A, light purple and light blue, respectively). Except for a slightly higher value for PAJ_FeN$_x$C$_y$ at 0.55 V_{RHE} and a slightly lower value for UNIPD_FeN$_x$C$_y$ at 0.79 V_{RHE}, their *S*-numbers barely depend on the potential. Such a trend aligns with what was observed for an Fe–N–C catalyst rich with Fe_3C@N–C (PAJ_Fe_3C@N–C) in Alkaline-RT in our previous work (Fig. 3A, grey).[15] The data of PAJ_FeN$_x$C$_y$ was published in another previous work in the form of electric charge-normalized Fe dissolution,[8] and the *S*-number of UNIPD_FeN$_x$C$_y$ is newly reported here. The *S*-numbers of PAJ_Fe_3C@N–C ($0.58 < E < 0.86$ V_{RHE}), UNIPD_FeN$_x$C$_y$ ($0.59 < E < 0.68$ V_{RHE}), and PAJ_FeN$_x$C$_y$ ($0.61 < E < 0.86$ V_{RHE}), in Alkaline-RT are $(0.8 \pm 0.3) \times 10^6$, $(1.3 \pm 0.6) \times 10^6$, and $(1.6 \pm 0.7) \times 10^6$, respectively. These reported *S*-numbers are of the same order of magnitude around 10^6, and their differences are within the error bar. The *S*-number being 10^6 means that on average every 10^6 times the ORR charge transfer occurs, an Fe ion is dissolved from the catalyst layer.[15] Additionally, the almost constant *S*-number interlinks the destabilization of the Fe species with the ORR catalytic cycle. Namely, the intermediates of the Fe species at one or more step(s) of the catalytic cycle are less stable than others, leading to a certain probability of Fe dissolution during each cycle. This degradation mechanism seems dominant for Fe–N–C catalysts in Alkaline-RT, as suggested by the unwavering trend of the *S*-number. However, the *S*-number's trend might vary with the conditions under which Fe–N–C catalysts are exposed.

Starting with the temperature effect on the trend of the *S*-number of Fe–N–C catalysts in alkaline media, Fig. 3B shows the *S*-numbers of PAJ_FeN$_x$C$_y$ in Alkaline-HT and Alkaline-RT (violet and light violet, respectively). Except for the data point at 0.9 V_{RHE} at HT, the rising temperature hardly changes the trend and value of the *S*-number or the ORR charge-normalized Fe dissolution, although the Fe concentration background before any electrochemical technique was indeed higher at HT than RT, suggesting a lower sensitivity detecting Fe dissolution at HT in base. Also, the post-AST dissolution data in Alkaline-HT has a high background, worsened signal-to-noise ratio, and greatly varied Fe dissolution peaks of the repeated steps at -20 mA cm^{-2} (see Fig. S1F and S3F in the ESI†), and thus such a data set is not suitable for calculating the *S*-number. In addition to PAJ_FeN$_x$C$_y$, another FeN$_x$C$_y$-rich Fe–N–C catalyst (CNRS_FeN$_x$C$_y$) was also tested in Alkaline-HT. The *S*-numbers of these two FeN$_x$C$_y$-rich Fe–N–C catalysts in Alkaline-HT follow the same trend (see Fig. 3C). The values stay almost constant in the *E* range between 0.81 and 0.63 V_{RHE}, while at 0.885 ± 0.015

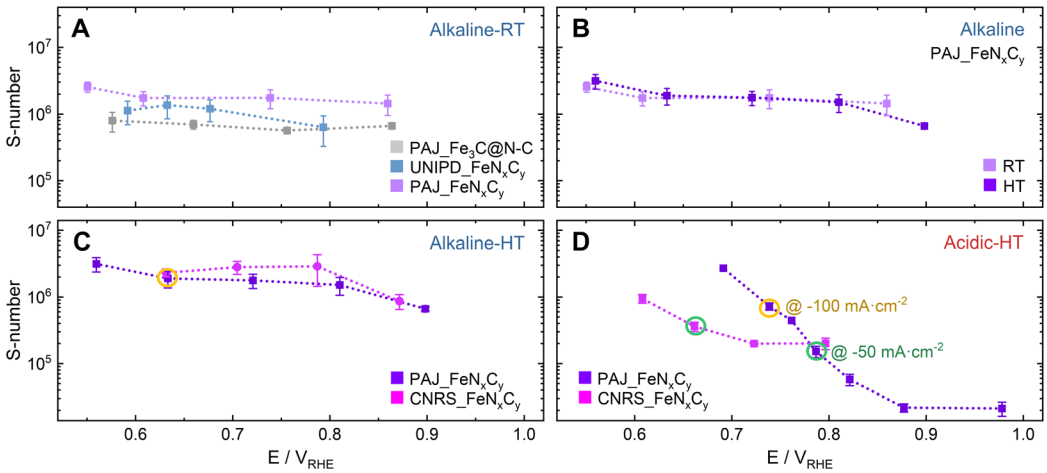

Fig. 3 The plots of *S*-number against the electrochemical potential (*E* V_{RHE}), where the *S*-number is defined as the number of electrons exchanged in the ORR per dissolved Fe cation. (A) A comparison of the *S*-numbers among three Fe–N–C catalysts, PAJ_Fe_3C@N–C (light grey), UNIPD_FeN_xC_y (light blue),[29] and PAJ_FeN_xC_y (light violet),[8] in 0.1 M NaOH at room temperature (RT); (B) a comparison of the *S*-numbers of PAJ_FeN_xC_y in 0.1 M NaOH at RT (light violet) and at 70 ± 6 °C (HT) (violet); (C & D) comparisons of the *S*-numbers between two Fe–N–C catalysts, CNRS_FeN_xC_y (magenta) and PAJ_FeN_xC_y (violet), (C) in 0.1 M NaOH at HT and (D) in 0.1 M $HClO_4$ at HT. The green and orange circles (the latter: only for PAJ_FeN_xC_y) mark the data points corresponding to the ORR current density at −50 mA cm^{-2} and at −100 mA cm^{-2}, respectively. The error bars represent the difference between the results of two experiments, and are mainly contributed by the unavoidable differences in the quality of the catalyst layers and the applied electrochemistry, as well as the detection limits of the ICP-MS. In (D), the two data points of PAJ_FeN_xC_y without error bars (at 0.69 and 0.76 V_{RHE}) are from only one measurement, but they also follow the trend of other data with error bars.

V_{RHE}, they are two to three times lower than those between 0.81 and 0.63 V_{RHE}. Therefore, the finding in Alkaline-RT that the amount of dissolved Fe during the ORR is highly correlated with the number of electrons exchanged in the ORR is still valid for FeN_xC_y-rich Fe–N–C catalysts at HT between 0.81 and 0.63 V_{RHE}.

The influence of the electrolyte pH value on the stability of FeN_xC_y sites at current densities from low values and up to −100 mA cm^{-2} is revealed by comparing the *S*-numbers of the FeN_xC_y-rich Fe–N–C catalysts in Alkaline-HT and Acidic-HT (compare Fig. 3C and D). Different from the trend of *S*-number observed in Alkaline-HT (see Fig. 3C), Fig. 3D reveals a trend of increasing stability (higher *S*-number) with decreasing potential (increasing current density). The *S*-numbers of CNRS_FeN_xC_y in Acidic-HT (Fig. 3D, magenta) in the potential range $0.66 \leq E \leq 0.80$ V_{RHE} are lower than its *S*-numbers in Alkaline-HT (Fig. 3C, magenta). This trend is also observed comparing the *S*-numbers of PAJ_FeN_xC_y in Acidic-HT in the potential range $0.79 \leq E \leq 0.98$ V_{RHE} and those in Alkaline-HT (Fig. 3D and C, violet). It is worth noting that the lower limits of the above-mentioned potential ranges (defined so that all *S*-numbers observed in acidic conditions are lower than *S*-numbers in alkaline conditions) are the potential values correspond to the ORR current density of −50 mA cm^{-2}, marked with green circles in Fig. 3D. Because a lower *S*-number suggests worse stability, the results indicate that the FeN_xC_y sites are much less stable in Acidic-HT at $|j| \leq 50$ mA cm^{-2} than in Alkaline-HT. Moreover, when $|j|$ is above 50 mA cm^{-2}, such as 100 mA cm^{-2} for PAJ_FeN_xC_y marked in orange circles in Fig. 3C and D, the *S*-number obtained in Acidic-HT is almost comparable to (only slightly lower than) that in Alkaline-HT. Hence, the FeN_xC_y sites are generally less stable in Acidic-HT than in Alkaline-HT at the ORR current densities up to −100 mA cm^{-2}, which at least partially explains the more severe degradation in the ORR performance after the AST in Acidic-HT *vs.* that after the AST in Alkaline-HT (Fig. 1).

Different from the steady *S*-numbers in Alkaline-RT and Alkaline-HT, the *S*-number obtained in Acidic-HT varies two orders of magnitude for PAJ_FeN_xC_y in the *E* range 0.9–0.7 V_{RHE} and one order of magnitude for CNRS_FeN_xC_y in the *E* range

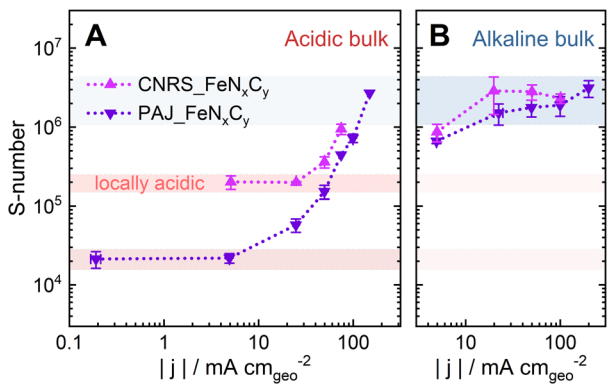

Fig. 4 The plots of the *S*-numbers of two Fe–N–C catalysts, PAJ_FeN_xC_y (violet) and CNRS_FeN_xC_y (magenta), against the absolute value of the ORR current density $|j|$ at 70 ± 6 °C (A) in 0.1 M $HClO_4$ and (B) in 0.1 M NaOH. Note that the *S*-number data in (A and B) is the same set as in Fig. 3D and C, respectively. The error bars represent the differences between the results of two measurements. The red and blue shades suggest the ranges of the *S*-number of the Fe–N–C catalysts when the catalyst layers are dominantly acidic and alkaline, respectively.

0.8–0.6 V_{RHE} (see Fig. 3D). Such considerable changes in the *S*-number in Acidic-HT indicate a poor correlation between the rates of Fe dissolution and the ORR charge transfer, and/or underlying mechanisms that depend on the electrochemical potential and/or the ORR current density. As mentioned in the introduction, three potential mechanisms include the ROS attack, the potential-dependence or -independence of the oxidation state of FeN_4C_y sites, and the increased local pH values at elevated ORR current densities. Because the impacts of the former two are specific to the species of FeN_xC_y sites and the influence of the latter is more general for various FeN_xC_y sites, in the following discussion section, we further explore how an elevated ORR current density may induce higher local pH values in the Fe–N–C catalyst layer in Acidic-HT and, subsequently, an increased *S*-number. For such a discussion, the *S*-number data in Fig. 3C and D is plotted against the absolute value of the ORR current density $|j|$ in a log–log scale as the plots in Fig. 4B and A, respectively.

4. Discussion

The trend of the *S*-number of the Fe–N–C catalysts in Acidic-HT may be at least partially attributed to an increased local pH value during the ORR, which consumes H^+. Our previous work[26] reported that from pH = 1 at the catalyst-layer/liquid-electrolyte interface of a 60 μm Fe–N–C/Nafion catalyst layer in a GDE half-cell, the local pH value may rise to above pH = 8 at the gas/catalyst-layer interface at −15 mA cm^{-2} (ORR current density) at RT. On the other hand, at almost 0 mA cm^{-2} (0.75 V_{RHE}) in Ar at RT, the calculated pH value in the catalyst layer barely shifts from pH = 1.[26] This comparison of the local pH values at 0 and −15 mA cm^{-2} emphasizes the influence of the ORR current density on the local pH value in a catalyst layer contacting an acidic electrolyte. In Fig. 4A, in low-current-density regions, where the local environment of the active sites stays acidic, the *S*-numbers of the two FeN_xC_y-rich Fe–N–C catalysts differ by one order of magnitude, $(2.2 \pm 0.5) \times 10^4$ for PAJ_FeN_xC_y ($0.2 \leq |j| \leq 5$ mA cm^{-2}) and $(2.0 \pm 0.4) \times 10^5$ for CNRS_FeN_xC_y ($5 \leq |j| \leq 25$ mA cm^{-2}). However, as the current density rises, they follow the same trend where the values stay almost constant in the low-current-density regions, start rising at around −25 mA cm^{-2} for PAJ_FeN_xC_y and at around −50 mA cm^{-2} for CNRS_FeN_xC_y, and then reach the order of magnitude observed in alkaline media around 10^6 (marked as the blue shade in Fig. 4). This trend in Fig. 4A coincides with the hypothesis that a higher current density may result in a higher local pH value in the catalyst layer. Then, the increased local pH could lead to a higher stability of the HO-FeN_xC_y species, an increased tendency for the dissolved Fe cations to redeposite as Fe oxide/hydroxide,[26] and thus, a higher *S*-number, which eventually approaches that observed in alkaline media.

In contrast, the *S*-numbers of the Fe–N–C catalysts in alkaline media hardly vary with electrochemical potential ($0.63 < E < 0.81$ V_{RHE}) or current density ($20 < |j| < 100$ mA cm^{-2}) (see Fig. 4B). Although the local pH value may also increase in alkaline catalyst layers during the ORR, which produces OH^-, the boundary condition at the catalyst-layer/electrolyte interface is already pH = 13. Increasing the pH value from pH = 13 to 14 requires a growth in the [OH^-] from 0.1 to 1 M, calling for a higher ORR current density than a case where the local pH increases from pH = 1 to 2, corresponding to a drop in [H^+] from 0.1 to 0.01 M. Thus, the impact of the ORR current density on the increase of the local pH value is less pronounced in alkaline media than in acidic media. Additionally, according to DFT calculations, the thermodynamically stable species at 0.6 V shifts from Fe^{2+} (Fe in FeN_xC_y being less stable than free Fe^{2+}) to HO–FeN_xC_y when the pH value increases from only 1 to 2. In contrast, at pH = 13, the HO–FeN_xC_y is already the dominant stable species.[27] Consequently, the stability of the HO–FeN_xC_y species can be greatly influenced by the ORR current density in acidic media but barely in alkaline media, agreeing with the trends of the *S*-number shown in Fig. 4.

The two bases of the proposed hypothesis explaining the significant influence of the ORR current density on the stability of FeN_xC_y active sites in Acidic-HT (or the trends of the *S*-numbers of FeN_xC_y-rich Fe–N–C catalysts in Acidic-HT in Fig. 4A) are that the elevated current density increases the local pH, and that the increased local pH stabilizes the FeN_xC_y active sites and increases the tendency towards Fe oxide/hydroxide redeposition.[26] While the latter is a well accepted knowledge of Fe–N–C catalysts,[14] the former is a recently introduced concept,[26] for which further validation is preferable before implementation. Hence, pH profiles of a 40-μm Fe–N–C catalyst layer are simulated at current densities up to −94 mA cm^{-2} with the initial pH value being 1. The kinetic model considered a 10-s CP step followed by an OCP step and was run independently 5 times with various current densities of the CP step (−3.3, −15, −38, −69, and −94 mA cm^{-2}) (see Fig. 5A). The model takes the following reactions into account: the ORR, the self-ionization of water, the Fe precipitation, and the Fe dissolution from FeN_xC_y sites (see Section 2.4). Additionally, the rate of Fe dissolution from Fe–N–C sites was set as the rate of ORR ($k_r \times C_H$) times a dissolution coefficient k_{dis} (see eqn (3) in Section 2.4) which is inversely proportional to *S*-number. Although *S*-number (or k_{dis}) is supposed to be a function of pH, this is still a missing data set and thus cannot yet be input in the current kinetic model. At the current stage, for this simulation set, the value of k_{dis} is set as 4.6×10^{-5}, the reciprocal of the *S*-number of PAJ_FeN_xC_y at current densities below −5 mA cm^{-2} (2.2×10^4, see Fig. 4A), to first show the increased local pH in the catalyst layer at elevated current densities. As a result, the simulated pH profiles in the catalyst layer at the end of the 10-s steps are shown in Fig. 5B, where the boundary conditions $x = 0$ and 40 μm correspond to the gas-phase/catalyst-layer interface and the catalyst-layer/liquid-electrolyte interface, respectively. The pH values in the catalyst layer generally rise with the increasing current density, verifying the hypothesis.

Although Fe precipitation is considered in the model, the pH-dependence of the *S*-number is not yet. The comparison between the simulation result and experimental data can reveal how the lack of such consideration leads to the discrepancy of the results. The Fe flux escaping from the catalyst layer is presented in Fig. 5C. Based on the model, the Fe flux expectedly

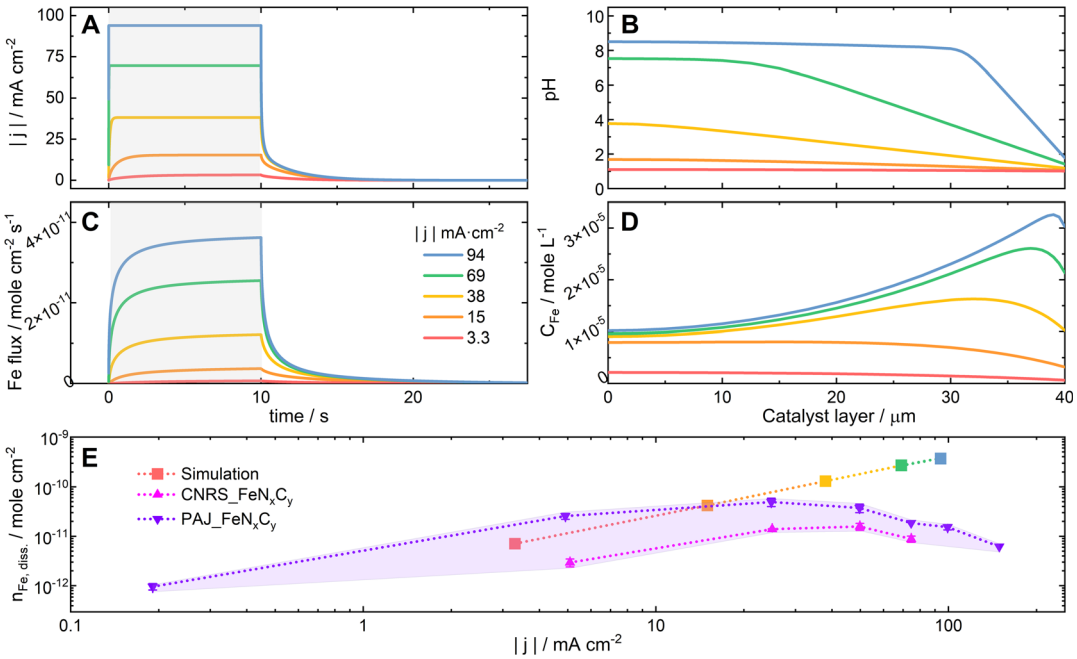

Fig. 5 Simulation of a 40 μm Fe–N–C catalyst layer, one side of which is in contact with an electrolyte of pH = 1 and the other with a gas diffusion layer. (A) The current density profiles experienced by the catalyst layer, including 10-s chronopotentiometry (CP) steps at various current densities followed by OCP steps. (B) The resulting pH profiles in the catalyst layer at the end of the 10-s steps. (C) The Fe flux escaping from the catalyst layer during and after the 10-s steps. (D) The profiles of the concentration of Fe^{m+} (C_{Fe}) in the catalyst layer at the end of the 10-s steps. (E) The amounts of the dissolved Fe during the 10-s steps at various current densities, which are integrated from the simulation data in (C) (square) and from the experimental data of CNRS_FeN_xC_y (magenta, up triangle) and PAJ_FeN_xC_y (violet, down triangle).

increases with the elevating current density. By integrating the Fe flux with respect to time, the simulated amounts of the dissolved Fe during these five steps are obtained and plotted against the current density of the corresponding step in the log–log scale in Fig. 5E (square symbol, the color corresponding to that of the same set of simulation data in Fig. 5A–D). The simulated amounts of the dissolved Fe species during the 10-s step at -94 mA cm^{-2} is 3.7×10^{-10} mole$_{Fe}$ cm^{-2} or 2.1×10^{-2} μg$_{Fe}$ cm^{-2}, which is around 0.3% of the Fe in an 1 cm^2 catalyst layer loaded with 1 mg Fe–N–C catalyst that contains 0.65 wt% Fe. Because the amount of the dissolved Fe during the considered protocol is relatively minute, the model considers the FeN_xC_y site density to be constant. From eqn (2), which was introduced in Section 2.3, the correlation between log$|j|$ and log($n_{Fe,diss.}$) can be written as eqn (7), suggesting that the theoretical slope of the simulation data in Fig. 5E is 1. Yet, the resulting slope of the simulation data is around 1.2. Its deviation from 1 can be at least partially attributed to the different mass transport (rate and direction) of the dissolved Fe species at varied current densities, which results from the different Fe concentration profiles in the catalyst layer (see Fig. 5D) and is considered in the kinetic model but not in eqn (7). For comparison, the experimentally acquired amounts of the dissolved Fe from PAJ_FeN_xC_y and CNRS_FeN_xC_y during the 10-s CP steps, which were used to calculate the *S*-numbers in Fig. 3D and 4A, are also plotted in Fig. 5E (violet and magenta triangular symbols, respectively).

$$\log n_{Fe,diss.} = \log|j| + \log(t/e/N_A) - \log(S\text{-number}) \quad (7)$$

Because the dependence of the *S*-number on the local pH value is not yet considered, the current model is limited to situations where the shift of the local pH values from 1 is still moderate. Otherwise, the simulation results would deviate from the experimental results. Indeed, when the current density is -3.3 mA cm^{-2}, the pH values in the catalyst layer barely shift from 1 (Fig. 5B, red), and the simulated amount of the dissolved Fe (Fig. 5E, red) falls in between the experimental results of PAJ_FeN_xC_y and CNRS_FeN_xC_y (shaded in light violet for visualization). Moreover, in the low-current-density regions ($|j| \leq 5$ mA cm^{-2} for PAJ_FeN_xC_y; $|j| \leq 25$ mA cm^{-2} for CNRS_FeN_xC_y), the slopes of the experimental data curves in Fig. 5E are similar to that of the simulation data. Hence, in this current density region, the model of using a constant *S*-number is valid, agreeing with the observation in Fig. 4A that the *S*-numbers of the Fe–N–C catalysts stay almost constant at low current densities. Next, when the current density is -15 mA cm^{-2}, the pH values in the catalyst layer have evidently shifted from 1 but are generally below 2 (Fig. 5B, orange). The slope of the experimental data curve of CNRS_FeN_xC_y in Fig. 5E at -15 mA cm^{-2} stays similar to the simulation one, while that of PAJ_FeN_xC_y has shifted lower. Interestingly, in Fig. 4A at -15 mA cm^{-2}, the *S*-number of CNRS_FeN_xC_y is still in its constant *S*-number region, while the *S*-number of PAJ_FeN_xC_y has potentially shifted away from its constant *S*-number region. Namely, the model is not always (or not entirely) valid at such a current density.

Furthermore, when the current density is above (not including) −15 mA cm^{-2}, the pH values in the catalyst layer have largely shifted away from 1 (Fig. 5B, yellow, green, and blue). In these cases, the simulation results generally deviate from the experimental results in Fig. 5E, and the *S*-numbers of both catalysts deviate from the constant *S*-number regions observed at low current densities in Fig. 4A. Although this model cannot yet predict the amounts of dissolved Fe at high current densities in acidic media, it emphasizes the importance of considering the dependence of the *S*-number of FeN_xC_y sites on the local pH value, and verifies that the pH values in the catalyst layer increase with the ORR current density (see Fig. 5B).

The linear correlation between the amount of the dissolved Fe species and the number of electrons exchanged in the ORR (the cumulative ORR faradaic charge divided by the elementary charge) at elevated current densities can still be examined by comparing the Fe dissolution during sub-protocols that applied the same current density, but implemented different step durations and cycle numbers. In the whole protocol, the 200-cycle AST and the step that applied the same elevated current density in the pre-AST activity test (−75 mA cm^{-2} for CNRS_FeN_xC_y in Acidic-HT, and −100 mA cm^{-2} for all the others) are the most suitable for such a comparison. Hence, the Fe dissolution data of PAJ_FeN_xC_y and CNRS_FeN_xC_y in both alkaline and acidic media during these sub-protocols is summarized in Fig. 6.

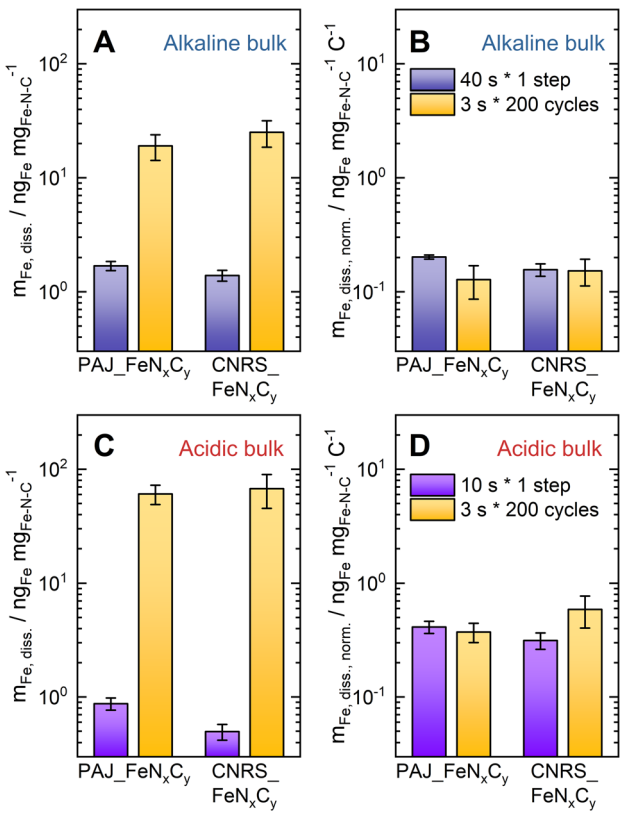

Fig. 6 The Fe dissolution data of PAJ_FeN_xC_y and CNRS_FeN_xC_y during the 200-cycle AST (each cycle: 3 s at "*j*" mA cm^{-2} and 3 s at −0.1 mA cm^{-2}, yellow bars) and the *t*-s galvanostatic step at "*j*" mA cm^{-2}. The duration *t* of the galvanostatic step is 40 s in alkaline media (A & B, indigo bars) or 10 s in acidic media (C & D, violet bars), and the current density "*j*" is −75 mA cm^{-2} for CNRS_FeN_xC_y in Acidic-HT, and −100 mA cm^{-2} for all the others (see Table 1). The amount of the dissolved Fe species has been normalized to the catalyst loading (A & C) or both the catalyst loading and the ORR charge (B & D). The error bars are equal to the differences between the results of the two measurements.

The amounts of the dissolved Fe species normalized to the loading ($m_{Fe,diss.}$ ng_{Fe} mg_{FeNC}^{-1}) during these sub-protocols in alkaline and acidic media are presented in Fig. 6A and C, respectively. Fig. 6A shows that the values of $m_{Fe,diss.}$ in alkaline media during the AST (yellow) are around one order of magnitude higher than those during the 40-s step (indigo). However, after further normalizing the $m_{Fe,diss.}$ values to the ORR charges (see $m_{Fe,diss.,norm.}$ ng_{Fe} mg_{FeNC}^{-1} C^{-1} in Fig. 6B), their values are almost the same for CNRS_FeN_xC_y and very close for PAJ_FeN_xC_y, considering the error bars. Eqn (8) shows that $m_{Fe,diss.,norm.}$ is inversely proportional to the *S*-number. Namely, their *S*-numbers during the AST are comparable to those pre-AST. This analysis verifies again the correlation between the amount of the dissolved Fe species and the number of electrons exchanged in the ORR, which has been reported for PAJ_Fe_3C@N–C and CNRS_FeN_xC_y in alkaline media at RT.[15] The slightly lower $m_{Fe,diss.,norm.}$ for PAJ_FeN_xC_y during the AST than that during the 40-s step can be attributed to a minor history effect. As for the acidic condition, Fig. 6C shows that the $m_{Fe,diss.}$ values during the AST (yellow) become around two orders of magnitude larger than those during the corresponding 10-s step (violet). Once more normalizing the $m_{Fe,diss.}$ values to the ORR charges (see Fig. 6D), the resulting values are similar for PAJ_FeN_xC_y and of the same magnitude for CNRS_FeN_xC_y. In other words, their *S*-numbers during the AST in Acidic-HT are similar to those obtained at the pre-AST galvanostatic step at the corresponding current density. This analysis suggests that in acidic media, the number of electrons exchanged in the ORR is also proportional to the amount of dissolved Fe from the FeN_xC_y-rich Fe–N–C catalysts when the applied current densities are the same. The equal ORR rates may lead to similar local pH values in the catalyst layers and, in turn, comparable stabilities of the FeN_xC_y sites and tendencies of Fe oxide/hydroxide redeposition. Consequently, the *S*-number for Fe–N–C catalysts in acidic media can also be meaningful when the impact of the applied current density on the local pH in catalyst layers and thus the *S*-number is considered.

$$m_{Fe,diss.,norm.} \times S\text{-number} = \frac{M_{Fe}}{10^{-9} \times N_A \times e \times \text{Loading} \times S_{GDE}} \quad (8)$$

where N_A, e, M_{Fe}, and S_{GDE} refer to the Avogadro constant, the elementary charge, the molar mass of Fe, and the geometric area of the GDE sample, respectively.

5. Conclusions and outlook

This work verifies the remarkable correlation between the rates of Fe dissolution and ORR charge transfer in alkaline media at both RT and 70 °C, regardless of the dominant Fe species, the

electrochemical potential (between 0.81 and 0.63 V_{RHE}), and the current density (up to -100 mA cm^{-2}) in the studied ranges. The resulting unwavering *S*-number in alkaline media suggests a certain probability of Fe leaching during each ORR catalytic cycle as a result of one or more intermediates of the Fe active sites present in both the ORR catalytic cycle and Fe dissolution process.[32] On the other hand, in acidic media at 70 °C, the almost constant *S*-number is so far only observed in a low-current-density region or for protocols at the same elevated current density. We attribute the dependence of the *S*-number on the current density in acidic media at least partially to the rising pH value in the catalyst layer induced by elevated ORR current densities, evidenced by kinetic modeling.

On the basis of this work, future works may further develop the following topics.

(a) Consider the pH-dependence of the *S*-number in the kinetic model: first, the *S*-numbers of Fe–N–C catalysts in different pH media at low current densities ($|j| \leq 5$ mA cm^{-2}) may be obtained using SFC-ICP-MS, which is more time-efficient than GDE-ICP-MS. Next, the experimentally acquired *S*-number as a function of pH can be incorporated into the kinetic model developed in this work to predict the amount of dissolved Fe at an elevated current density in acidic electrolytes. Then, the simulation results can be compared with the Fe dissolution data obtained with GDE-ICP-MS to further discuss the degradation mechanisms of Fe–N–C catalysts at elevated current densities. Note that for a long-term operation, the change in the site density over time should be considered in the kinetic model.

(b) Experimentally probe the local pH in (or close to) GDE samples during the ORR: for example, the probe electrode in scanning electrochemical microscopy (SECM) can be developed as a voltammetric pH sensor to reveal the local pH in close proximity to a GDE sample during the ORR.[33] Yet, SECM could not reveal the pH within the catalyst layers. On the other hand, using confocal microscopy and a pH-sensitive two-color fluorescent dye can offer the local pH profiles in catalyst layers, but it may be questionable if and how the dye interferes with the electrochemistry.[34] Hence, the method development for probing the local pH "in" catalyst layers, especially the thick ones, at elevated current densities without interfering with the electrochemistry is still required. In such future works, the experimental results and simulation data can be compared and discussed.

(c) Investigate the trend of *S*-number during a long-term operation: because the composition of the Fe species may vary over a long-term operation, the stability of Fe–N–C catalysts may as well. While the pre- and post-AST *S*-numbers of Fe–N–C catalysts in Acidic-HT are compared and discussed in Fig. S5 and the Supporting discussion in the ESI,† the *S*-number of Fe–N–C catalysts mainly with Fe oxides or Fe hydroxides should be obtained in a following work before the evolution trend of *S*-number of benchmark Fe–N–C catalysts during a long-term operation may be meaningfully discussed.

(d) Compare Fe dissolution from Fe–N–C catalysts in O_2- and Ar-purged acidic media in a GDE setup: such a comparison has been carried out in acidic media in a rotating disk electrode half-cell (RDE),[20] and in alkaline media in both RDE and GDE half-cells.[15,19] Yet, it has not been done in acidic media in a GDE setup, where elevated ORR current densities are reachable, while such a study may provide more fundamental insights to how Fe–N–C catalysts degrade.

(e) Use other representative single-atom catalysts[18,35–44] to further benchmark and develop best practices of the application of the *S*-number to generalize the findings of this work.

Data availability

All supporting data are provided in this paper.

Author contributions

Yu-Ping Ku: GDE-ICP-MS experimental design and measurement, data curation, formal analysis, scientific discussion, writing of original draft Kavita Kumar: GDE-ICP-MS experimental design and measurement, scientific discussion, editing Pierre Antoine Bonnefont: kinetic modeling, scientific discussion, editing Li Jiao: synthesis of the Fe–N–C catalyst CNRS_FeN_xC_y; Marco Mazzucato: synthesis of the Fe–N–C catalyst UNIPD_FeN_xC_y Christian Durante: scientific discussion, editing Frédéric Jaouen: scientific discussion, editing Serhiy Cherevko: project conceptualization and administration, validation, scientific discussion, editing.

Conflicts of interest

The authors declare no conflict of interest.

Acknowledgements

YPK acknowledges Jonas Möller for software development for data analysis, and Matej Zlatar, Tatiana Priamushko, and Christian Göllner for technical support during ICP-MS measurements. FJ acknowledges financial support from the French National Research Agency through the DEEP project (grant number ANR-21-CE05-0021). CD acknowledges MIUR for the project financed by the European Union – Next Generation EU – Bando PRIN 2022 PNRR – M4.C2.1.1: Progetto: P2022WANKS – ECHO-EF.

References

1 K. Kumar, L. Dubau, F. Jaouen and F. Maillard, Review on the Degradation Mechanisms of Metal-N-C Catalysts for the Oxygen Reduction Reaction in Acid Electrolyte: Current Understanding and Mitigation Approaches, *Chem. Rev.*, 2023, **123**(15), 9265–9326.

2 J. Kim, J. Lee and Y. Tak, Relationship between carbon corrosion and positive electrode potential in a proton-exchange membrane fuel cell during start/stop operation, *J. Power Sources*, 2009, **192**(2), 674–678.

3 Y. Yi, G. Weinberg, M. Prenzel, M. Greiner, S. Heumann, S. Becker and R. Schlögl, Electrochemical corrosion of a glassy carbon electrode, *Catal. Today*, 2017, **295**, 32–40.

4 K. Zhao, S. Han, L. Ke, X. Wu, X. Yan, X. Cao, L. Li, X. Jiang, Z. Wang, H. Liu and N. Yan, Operando Studies of Electrochemical Denitrogenation and Its Mitigation of N-Doped Carbon Catalysts in Alkaline Media, *ACS Catal.*, 2023, **13**(5), 2813–2821.

5 V. Goellner, C. Baldizzone, A. Schuppert, M. T. Sougrati, K. J. J. Mayrhofer and F. Jaouen, Degradation of Fe/N/C catalysts upon high polarization in acid medium, *Phys. Chem. Chem. Phys.*, 2014, **16**(34), 18454–18462.

6 K. Kumar, P. Gairola, M. Lions, N. Ranjbar-Sahraie, M. Mermoux, L. Dubau, A. Zitolo, F. Jaouen and F. Maillard, Physical and Chemical Considerations for Improving Catalytic Activity and Stability of Non-Precious-Metal Oxygen Reduction Reaction Catalysts, *ACS Catal.*, 2018, **8**(12), 11264–11276.

7 I. Martinaiou, A. Shahraei, F. Grimm, H. Zhang, C. Wittich, S. Klemenz, S. J. Dolique, H.-J. Kleebe, R. W. Stark and U. I. Kramm, Effect of metal species on the stability of Me-N-C catalysts during accelerated stress tests mimicking the start-up and shut-down conditions, *Electrochim. Acta*, 2017, **243**, 183–196.

8 Y.-P. Ku, K. Kumar, A. Hutzler, C. Götz, M. Vorochta, M. T. Sougrati, V. Lloret, K. Ehelebe, K. J. J. Mayrhofer, S. Thiele, I. Khalakhan, T. Böhm, F. Jaouen and S. Cherevko, Impact of Carbon Corrosion and Denitrogenation on the Deactivation of Fe–N–C Catalysts in Alkaline Media, *ACS Catal.*, 2024, **14**(11), 8576–8591.

9 C. H. Choi, C. Baldizzone, J.-P. Grote, A. K. Schuppert, F. Jaouen and K. J. J. Mayrhofer, Stability of Fe-N-C Catalysts in Acidic Medium Studied by Operando Spectroscopy, *Angew. Chem., Int. Ed.*, 2015, **54**(43), 12753–12757.

10 A. Serov, M. J. Workman, K. Artyushkova, P. Atanassov, G. McCool, S. McKinney, H. Romero, B. Halevi and T. Stephenson, Highly stable precious metal-free cathode catalyst for fuel cell application, *J. Power Sources*, 2016, **327**, 557–564.

11 C. H. Choi, H.-K. Lim, M. W. Chung, G. Chon, N. Ranjbar Sahraie, A. Altin, M.-T. Sougrati, L. Stievano, H. S. Oh, E. S. Park, F. Luo, P. Strasser, G. Dražić, K. J. J. Mayrhofer, H. Kim and F. Jaouen, The Achilles' heel of iron-based catalysts during oxygen reduction in an acidic medium, *Energy Environ. Sci.*, 2018, **11**(11), 3176–3182.

12 C. H. Choi, W. S. Choi, O. Kasian, A. K. Mechler, M. T. Sougrati, S. Brüller, K. Strickland, Q. Jia, S. Mukerjee, K. J. J. Mayrhofer and F. Jaouen, Unraveling the Nature of Sites Active toward Hydrogen Peroxide Reduction in Fe-N-C Catalysts, *Angew. Chem., Int. Ed.*, 2017, **56**(30), 8809–8812.

13 G. Bae, M. W. Chung, S. G. Ji, F. Jaouen and C. H. P. H. Choi, Effect on the H_2O_2-Induced Deactivation of Fe-N-C Catalysts, *ACS Catal.*, 2020, **10**(15), 8485–8495.

14 P. G. Santori, F. D. Speck, J. Li, A. Zitolo, Q. Jia, S. Mukerjee, S. Cherevko and F. Jaouen, Effect of Pyrolysis Atmosphere and Electrolyte pH on the Oxygen Reduction Activity, Stability and Spectroscopic Signature of FeN_x Moieties in Fe-N-C Catalysts, *J. Electrochem. Soc.*, 2019, **166**(7), F3311.

15 Y.-P. Ku, K. Ehelebe, A. Hutzler, M. Bierling, T. Böhm, A. Zitolo, M. Vorokhta, N. Bibent, F. D. Speck, D. Seeberger, I. Khalakhan, K. J. J. Mayrhofer, S. Thiele, F. Jaouen and S. Cherevko, Oxygen Reduction Reaction in Alkaline Media Causes Iron Leaching from Fe–N–C Electrocatalysts, *J. Am. Chem. Soc.*, 2022, **144**(22), 9753–9763.

16 J. Li, M. T. Sougrati, A. Zitolo, J. M. Ablett, I. C. Oğuz, T. Mineva, I. Matanovic, P. Atanassov, Y. Huang, I. Zenyuk, A. Di Cicco, K. Kumar, L. Dubau, F. Maillard, G. Dražić and F. Jaouen, Identification of durable and non-durable FeN_x sites in Fe–N–C materials for proton exchange membrane fuel cells, *Nat. Catal.*, 2021, **4**(1), 10–19.

17 J. Herranz, F. Jaouen, M. Lefèvre, U. I. Kramm, E. Proietti, J.-P. Dodelet, P. Bogdanoff, S. Fiechter, I. Abs-Wurmbach, P. Bertrand, T. M. Arruda and S. Mukerjee, Unveiling N-Protonation and Anion-Binding Effects on Fe/N/C Catalysts for O_2 Reduction in Proton-Exchange-Membrane Fuel Cells, *J. Phys. Chem. C*, 2011, **115**(32), 16087–16097.

18 S. Liu, C. Li, M. J. Zachman, Y. Zeng, H. Yu, B. Li, M. Wang, J. Braaten, J. Liu, H. M. Meyer, M. Lucero, A. J. Kropf, E. E. Alp, Q. Gong, Q. Shi, Z. Feng, H. Xu, G. Wang, D. J. Myers, J. Xie, D. A. Cullen, S. Litster and G. Wu, Atomically dispersed iron sites with a nitrogen–carbon coating as highly active and durable oxygen reduction catalysts for fuel cells, *Nat. Energy*, 2022, **7**(7), 652–663.

19 R. Sgarbi, K. Kumar, V. A. Saveleva, L. Dubau, R. Chattot, V. Martin, M. Mermoux, P. Bordet, P. Glatzel, E. A. Ticianelli, F. Jaouen and F. Maillard, Electrochemical Transformation of Fe-N-C catalysts into Iron Oxides in Alkaline Medium and Its Impact on the Oxygen Reduction Reaction Activity, *Appl. Catal., B*, 2022, **311**, 121366.

20 K. Kumar, L. Dubau, M. Mermoux, J. Li, A. Zitolo, J. Nelayah, F. Jaouen and F. Maillard, On the Influence of Oxygen on the Degradation of Fe-N-C Catalysts, *Angew. Chem.*, 2020, **132**(8), 3261–3269.

21 G. Bae, M. M. Kim, M. H. Han, J. Cho, D. H. Kim, M.-T. Sougrati, J. Kim, K.-S. Lee, S. H. Joo, W. A. Goddard, H.-S. Oh, H. Kim, F. Jaouen and C. H. Choi, Unravelling the complex causality behind Fe–N–C degradation in fuel cells, *Nat. Catal.*, 2023, **6**(12), 1140–1150.

22 S. Geiger, O. Kasian, M. Ledendecker, E. Pizzutilo, A. M. Mingers, W. T. Fu, O. Diaz-Morales, Z. Li, T. Oellers, L. Fruchter, A. Ludwig, K. J. J. Mayrhofer, M. T. M. Koper and S. Cherevko, The stability number as a metric for electrocatalyst stability benchmarking, *Nat. Catal.*, 2018, **1**(7), 508–515.

23 O. Kasian, J.-P. Grote, S. Geiger, S. Cherevko and K. J. J. Mayrhofer, The Common Intermediates of Oxygen Evolution and Dissolution Reactions during Water Electrolysis on Iridium, *Angew. Chem., Int. Ed.*, 2018, **57**(9), 2488–2491.

24 M. M. Hossen, K. Artyushkova, P. Atanassov and A. Serov, Synthesis and characterization of high performing Fe-N-C

catalyst for oxygen reduction reaction (ORR) in Alkaline Exchange Membrane Fuel Cells, *J. Power Sources*, 2018, **375**, 214–221.

25 X. Tan, H. A. Tahini and S. C. Smith, Unveiling the role of carbon oxidation in irreversible degradation of atomically-dispersed FeN_4 moieties for proton exchange membrane fuel cells, *J. Mater. Chem. A*, 2021, **9**(13), 8721–8729.

26 A. Pedersen, K. Kumar, Y.-P. Ku, V. Martin, L. Dubau, K. T. Santos, J. Barrio, V. A. Saveleva, P. Glatzel, V. K. Paidi, X. Li, A. Hutzler, M.-M. Titirici, A. Bonnefont, S. Cherevko, I. E. L. Stephens and F. Maillard, Operando Fe dissolution in Fe–N–C electrocatalysts during acidic oxygen reduction: impact of local pH change, *Energy Environ. Sci.*, 2024, **17**(17), 6323–6337.

27 E. F. Holby, G. Wang and P. Zelenay, Acid Stability and Demetalation of PGM-Free ORR Electrocatalyst Structures from Density Functional Theory: A Model for "Single-Atom Catalyst" Dissolution, *ACS Catal.*, 2020, **10**, 14527–14539.

28 H. Adabi, P. G. Santori, A. Shakouri, X. Peng, K. Yassin, I. G. Rasin, S. Brandon, D. R. Dekel, N. U. Hassan, M.-T. Sougrati, A. Zitolo, J. R. Varcoe, J. R. Regalbuto, F. Jaouen and W. E. Mustain, Understanding how single-atom site density drives the performance and durability of PGM-free Fe–N–C cathodes in anion exchange membrane fuel cells, *Mater. Today Adv.*, 2021, **12**, 100179.

29 M. Mazzucato, G. Daniel, A. Mehmood, T. Kosmala, G. Granozzi, A. Kucernak and C. Durante, Effects of the induced micro- and meso-porosity on the single site density and turn over frequency of Fe-N-C carbon electrodes for the oxygen reduction reaction, *Appl. Catal., B*, 2021, **291**, 120068.

30 K. Ehelebe, J. Knöppel, M. Bierling, B. Mayerhöfer, T. Böhm, N. Kulyk, S. Thiele, K. J. J. Mayrhofer and S. Cherevko, Platinum Dissolution in Realistic Fuel Cell Catalyst Layers, *Angew. Chem., Int. Ed.*, 2021, **60**(16), 8882–8888.

31 K. Kumar, T. Asset, X. Li, Y. Liu, X. Yan, Y. Chen, M. Mermoux, X. Pan, P. Atanassov, F. Maillard and L. Dubau, Fe–N–C Electrocatalysts' Durability: Effects of Single Atoms' Mobility and Clustering, *ACS Catal.*, 2020, **11**(2), 484–494.

32 S. Gottesfeld, Editors' Choice—Review—Polymer Electrolyte Fuel Cell Science and Technology: Highlighting a General Mechanistic Pattern and a General Rate Expression for Electrocatalytic Processes, *J. Electrochem. Soc.*, 2022, **169**(12), 124518.

33 T. Quast, S. Dieckhöfer and W. Schuhmann, Spearhead Metal Ultramicroelectrodes Based on Carbon Nanoelectrodes as Local Voltammetric pH Sensors, *Electrochem. Sci. Adv.*, 2025, e70004.

34 A. J. Welch, A. Q. Fenwick, A. Böhme, H.-Y. Chen, I. Sullivan, X. Li, J. S. DuChene, C. Xiang and H. A. Atwater, Operando Local pH Measurement within Gas Diffusion Electrodes Performing Electrochemical Carbon Dioxide Reduction, *J. Phys. Chem. C*, 2021, **125**(38), 20896–20904.

35 L. Jiao, J. Li, L. L. Richard, Q. Sun, T. Stracensky, E. Liu, M. T. Sougrati, Z. Zhao, F. Yang, S. Zhong, H. Xu, S. Mukerjee, Y. Huang, D. A. Cullen, J. H. Park, M. Ferrandon, D. J. Myers, F. Jaouen and Q. Jia, Chemical vapour deposition of Fe–N–C oxygen reduction catalysts with full utilization of dense Fe–N_4 sites, *Nat. Mater.*, 2021, **20**(10), 1385–1391.

36 F. Luo, A. Roy, L. Silvioli, D. A. Cullen, A. Zitolo, M. T. Sougrati, I. C. Oguz, T. Mineva, D. Teschner, S. Wagner, J. Wen, F. Dionigi, U. I. Kramm, J. Rossmeisl, F. Jaouen and P. Strasser, P-block single-metal-site tin/nitrogen-doped carbon fuel cell cathode catalyst for oxygen reduction reaction, *Nat. Mater.*, 2020, **19**(11), 1215–1223.

37 H. Jin, R. Yu, P. Ji, W. Zeng, Z. Li, D. He and S. Mu, Sharply expanding single-atomically dispersed Fe–N active sites through bidirectional coordination for oxygen reduction, *Chem. Sci.*, 2024, **15**(19), 7259–7268.

38 H. Jin, J. Zhu, R. Yu, W. Li, P. Ji, L. Liang, B. Liu, C. Hu, D. He and S. Mu, Tuning the Fe–N_4 sites by introducing Bi–O bonds in a Fe–N–C system for promoting the oxygen reduction reaction, *J. Mater. Chem. A*, 2022, **10**(2), 664–671.

39 J. Zhu and S. Mu, Active site engineering of atomically dispersed transition metal–heteroatom–carbon catalysts for oxygen reduction, *Chem. Commun.*, 2021, **57**(64), 7869–7881.

40 Q. Ma, H. Jin, J. Zhu, Z. Li, H. Xu, B. Liu, Z. Zhang, J. Ma and S. Mu, Stabilizing Fe–N–C Catalysts as Model for Oxygen Reduction Reaction, *Advanced Science*, 2021, **8**(23), 2102209.

41 X. Xie, C. He, B. Li, Y. He, D. A. Cullen, E. C. Wegener, A. J. Kropf, U. Martinez, Y. Cheng, M. H. Engelhard, M. E. Bowden, M. Song, T. Lemmon, X. S. Li, Z. Nie, J. Liu, D. J. Myers, P. Zelenay, G. Wang, G. Wu, V. Ramani and Y. Shao, Performance enhancement and degradation mechanism identification of a single-atom Co–N–C catalyst for proton exchange membrane fuel cells, *Nat. Catal.*, 2020, **3**(12), 1044–1054.

42 X. Yang, M. Wang, M. J. Zachman, H. Zhou, Y. He, S. Liu, H.-Y. Zang, Z. Feng and G. Wu, Binary Atomically Dispersed Metal-Site Catalysts with Core–Shell Nanostructures for O_2 and CO_2 Reduction Reactions, *Small Sci.*, 2021, **1**(10), 2100046.

43 D. Malko, T. Lopes, E. Symianakis and A. R. Kucernak, The intriguing poison tolerance of non-precious metal oxygen reduction reaction (ORR) catalysts, *J. Mater. Chem. A*, 2016, **4**(1), 142–152.

44 M. Primbs, Y. Sun, A. Roy, D. Malko, A. Mehmood, M.-T. Sougrati, P.-Y. Blanchard, G. Granozzi, T. Kosmala, G. Daniel, P. Atanassov, J. Sharman, C. Durante, A. Kucernak, D. Jones, F. Jaouen and P. Strasser, Establishing reactivity descriptors for platinum group metal (PGM)-free Fe–N–C catalysts for PEM fuel cells, *Energy Environ. Sci.*, 2020, **13**(8), 2480–2500.